

OPEN ACCESS

Mechanically Coupled Phase-Field Modeling of Microstructure Evolution in Sodium Ion Batteries Particles of $Na_x FePO_4$

To cite this article: Tao Zhang and Marc Kamlah 2020 *J. Electrochem. Soc.* **167** 020508

View the [article online](#) for updates and enhancements.



Mechanically Coupled Phase-Field Modeling of Microstructure Evolution in Sodium Ion Batteries Particles of Na_xFePO_4

Tao Zhang^z and Marc Kamlah

Institute for Applied Materials, Karlsruhe Institute of Technology, 76344 Eggenstein-Leopoldshafen, Germany

The microstructure evolution of the cathode material Na_xFePO_4 of sodium-ion batteries is investigated during insertion, using a mechanically coupled phase-field model. A direct comparison between Na_xFePO_4 and Li_xFePO_4 is made in terms of the microstructure evolution and the stress evolution. The dynamics of single wave propagation in spherical particles of Na_xFePO_4 is obtained, and the interface morphology between phases that goes across the particle dynamically changes to minimize its proportion. When mechanics is accounted for, the interface gets more widened for Na_xFePO_4 , and its miscibility gap is significantly reduced. In contrast to the constant stresses in each phase occurring in shrinking-core dynamics, both, tensile and compressive stresses coexist in each phase, and the related gradient of hydrostatic stress induces Na_xFePO_4 a steeper concentration inhomogeneity in each phase. It is expected that the particle surface of the species-rich phase is more prone to cracking. Compared with Li_xFePO_4 , the stress magnitudes at the interface are smaller in Na_xFePO_4 . Although the miscibility gap of Na_xFePO_4 is smaller, the stress magnitudes at the particle surface are larger in this material, which makes it less mechanically reliable.

© 2020 The Author(s). Published on behalf of The Electrochemical Society by IOP Publishing Limited. This is an open access article distributed under the terms of the Creative Commons Attribution 4.0 License (CC BY, <http://creativecommons.org/licenses/by/4.0/>), which permits unrestricted reuse of the work in any medium, provided the original work is properly cited. [DOI: 10.1149/1945-7111/ab645a]



Manuscript submitted November 8, 2019; revised manuscript received December 12, 2019. Published January 9, 2020.

Sodium-ion batteries (NIBs) have been considered as a promising alternative to Lithium-ion batteries (LIBs), since sodium is widely available and relatively cheaper, while it exhibits similar chemical properties to lithium.¹ Due to the thermal stability and higher voltage, phosphate based cathode materials are regarded as one of the best candidates among all cathode materials for NIBs.² Compared to the other phosphate polyanion cathode materials, olivine Na_xFePO_4 (NaFPO) has the highest theoretical specific capacity.² Although olivine NaFPO has the same phase structure as olivine Li_xFePO_4 (LiFPO) of LIBs, the phase segregation thermodynamics for sodium-ion insertion in NaFPO are quite different from the lithiation process in LiFPO.^{1,3–6} In contrast to LiFPO, where transformation from a lithium-poor phase $FePO_4$ into a lithium-rich phase $LiFePO_4$ occurs directly, the system of NaFPO goes through an intermediate state at $Na_{2/3}FePO_4$.⁵ At room temperature, for $0 < x < 2/3$, phase segregation of olivine NaFPO into a sodium-poor phase $FePO_4$ and a sodium-rich phase $Na_{2/3}FePO_4$ is found to be favorable. For $2/3 < x < 1$, there is a solid-solution phase Na_xFePO_4 that is a single-phase region. In addition, the volume expansion of $FePO_4$ upon sodiation to $NaFePO_4$ can reach about 17%, and even the volume expansion from $FePO_4$ to $Na_{2/3}FePO_4$ is still quite large (about 12.8%), which is nearly 2 times that for LiFPO (about 6.8%) upon full lithium insertion.⁵ For the phase separating cathode materials, a volume mismatch between the species-poor phase and the species-rich phase may induce large concentration gradients at a mesoscopic scale and thus also large stress magnitudes, which can cause particle fracture and capacity loss.^{7–12} On the other hand, for thermodynamical reasons, there is a contribution of the stresses to the driving force for diffusion in the host material.^{13–19}

The description of diffusion and phase changes within an electrode material can be modeled by the Cahn–Hilliard theory. A thermodynamic phase-field model based on the Cahn–Hilliard equation relies on a continuous order parameter which is a conserved quantity, thus, leading to diffuse interfaces between adjacent phases with no need for the cumbersome tracking of the position of a sharp interface.²⁰ Our recent work²¹ has investigated the nonlocality of the Cahn–Hilliard theory, and demonstrated that it is weakly nonlocal. Huttin and Kamlah²² considered the 1D mechanically coupled Cahn–Hilliard equation for spherical particles of $Li_xMn_2O_4$ (LMO) of LIBs, and reveal that large stresses may also occur even at low C-rates. Zeng and Bazant²³ employed the 1D spherically symmetric

phase field model without mechanics to investigate high C-rates in a spherical nanoparticle made of LiFPO. A phase-field model for NaFPO of SIBs is studied for the first time in our recent work²⁴ for the spherically symmetric boundary value problem. This work captures the important feature of phase segregation into the sodium-poor phase $FePO_4$ and the sodium-rich phase $Na_{2/3}FePO_4$.

The above 1D works^{22–24} are limited to the shrinking-core concept, where the interface between two phases would not intersect with the particle surface and moves parallel to the species flux direction. However, experimental observations show that the classical “core–shell” structure can be destroyed.^{25–28} Santoki et al.²⁹ used the 2D Cahn–Hilliard theory without mechanics to study the mesoscopic effect of the surface curvature of the cathodic particle made of LMO. They reveal that, at a C-rate of $C = 1$, the “core–shell” structure even occurs in an irregularly shaped particle. Zhao et al.³⁰ derived a Cahn–Hilliard phase-field model coupled to mechanics based on Neo-Hookean elasticity, and only one eighth of the whole 3D electrode particle is considered due to the symmetry. They show that the “core–shell” structure forms in 3D spheroidal particles.

In order to relax the constraint of the “core–shell” structure, Singh et al.³¹ developed a general continuum theory without mechanics for phase-transformation dynamics by coupling an anisotropic Cahn–Hilliard phase-field model with surface reactions. This theory predicts a new regime of surface-reaction-limited dynamics, where the phase boundary extends from surface to surface in LiFPO particles. Subsequently, Cogswell and Bazant³² incorporated the influence of the elastic strain energy into the above surface-reaction-limited phase-field model. They performed the phase-field simulations by allowing a square particle at a stage of average concentration of $c_{avg} = 0.5$ to relax to equilibrium at zero current. Not looking at other average concentration values, the microstructure evolution during a time dependent insertion process is not taken into account. Later, Bazant’s group developed dynamical mechanically coupled phase-field models for the cathode materials LiFPO³³ and Li_xCoO_2 ³⁴ of LIBs, which goes beyond considering just the relaxation at a constant average filling. Di Leo et al.³⁵ formulated a continuum model which coupled the Cahn–Hilliard-type phase-field theory with finite deformation elasticity, and studied the coupled chemo-mechanical problem of lithiation of a spheroidal LiFPO particle. Based on 2D quarter particle model accounting for both, the radial symmetry and mirror symmetry, they find that, at a slow ramp of the externally applied electrochemical potential, a mildly curved “planar front” separates two phases. Welland et al.³⁶ later developed a 3D comprehensive phase-field model with the coupling to mechanics and investigated equilibrium states of LiFPO spherical

^zE-mail: tao.zhang@kit.edu

particles for different average lithium concentration. Their 3D simulations show that asymmetric phase-segregation forms in the spherical particles at the equilibrium states. However, no flux is applied at the surface of the particles in their work, rather a phase segregated concentration profile or a fluctuation field was used as an initial condition for different surface wetting cases. They have not yet addressed the dynamic loading, which is related to the experimentally more relevant condition of a constant applied flux. What is more, they do not investigate the stress evolution during insertion, which plays a nontrivial role in the electrode performance.

It should be noticed that the mirror symmetry of the model is taken into account in the above works.^{30,35} From the viewpoint of physics, there is no need that the concentration field satisfies such constraint of mirror symmetry. The only physical condition is that the free energy has to diminish when the system relaxes toward equilibrium. The question is still open how the model dimensionality and mirror symmetry affect the microstructure evolution of intercalation electrode materials. On the other hand, as far as we know, neither the experimental reports nor the theoretical works have disclosed how the microstructure of the cathode material NaFPO evolves during sodium insertion by now. Furthermore, it is very interesting to make a direct comparison between NaFPO and LiFPO in terms of the evolution of microstructure and stresses.

In this work, a mechanically coupled phase-field model is derived to investigate the microstructure evolution of NaFPO. The 2D simulation of the time dependent insertion process in electrode particles including the coupling to mechanics is achieved using the advanced numerical technologies of mesh adaptivity and time step adaptivity, as well as parallelization. We will investigate the influences of the model dimensionality and mirror symmetry, and reveal the microstructure evolution of NaFPO. We will also study how the mechanical stress affects the microstructure evolution of NaFPO.

The Paper is organized as follows. In Theory section, we present the mechanically coupled Cahn–Hilliard theory. The governing equations, boundary conditions, and material parameters are summarized. The resulting set of equations is implemented in the finite-element, multiphysics framework MOOSE³⁷ for the solution of the initial-boundary-value problem. We first validate the MOOSE implementation, and investigate the influences of the model dimensionality and mirror symmetry, then compare the microstructure evolution of NaFPO to that of LiFPO for the diffusion cases without and with mechanics in Results and Discussion section. Finally, we conclude our study in Conclusion section.

Theory

The mechanically coupled Cahn–Hilliard theory.—The Cahn–Hilliard phase-field model coupled with mechanics will be motivated now. In the phase-field model, we introduce as an order parameter, depending continuously on space, the species concentration c , which is measured in mol per unit volume. The system free energy of some domain of volume V accounting for mechanics is given by³⁸

$$\begin{aligned} \Psi(c, \text{grad } c, \varepsilon) &= \int_B \psi(c, \text{grad } c, \varepsilon) dV \\ &= \int_B (\psi^{mwp}(c) + \psi^{gd}(\text{grad } c) + \psi^{cp}(\varepsilon, c)) dV, \end{aligned} \quad [1]$$

where ψ^{mwp} , ψ^{gd} , and ψ^{cp} are the homogeneous free energy density, the gradient energy density, and the coupling energy density, respectively.

The homogeneous free energy density ψ^{mwp} is a multiwell potential defining the respective phases, which can be represented by

$$\begin{aligned} \psi^{mwp}(\bar{c}) &= k_B T_{ref} N_A c_{max} \left(\alpha_1 \bar{c} + \frac{\alpha_2}{2} \bar{c}^2 \right. \\ &\quad \left. + \frac{T}{T_{ref}} \left(\bar{c} \ln \bar{c} + \left(\frac{2}{3} - \bar{c} \right) \ln \left(\frac{2}{3} - \bar{c} \right) \right) \right), \end{aligned} \quad [2]$$

where \bar{c} is the dimensionless concentration, normalized with respect to the maximum species concentration c_{max} as $\bar{c} = c/c_{max}$. This is the classical multiwell potential function for a two phase material,^{22,39} which we have formulated such that it is limited to the two-phase region of NaFPO. Here, k_B , N_A , and T_{ref} are the Boltzmann constant, Avogadro constant, and reference temperature, respectively. The first two terms on the right hand side of Eq. 2 represent the interaction energy, where positive values of α_1 characterize the energy of inserting a species into the host material, and negative values of α_2 indicate the interaction of neighboring species to be attractive. At $T = T_{ref}$ the attraction is strong enough to initiate phase segregation for $\alpha_2 < -4$. The terms multiplied by absolute temperature T represent the entropy of mixing.^{30,40}

The gradient energy density leading to a diffuse interface between two adjacent phases is expressed as

$$\psi^{gd}(\text{grad } \bar{c}) = k_B T_{ref} N_A c_{max} \left(\frac{1}{2} \lambda |\text{grad } \bar{c}|^2 \right), \quad [3]$$

where λ is a material constant with units of length squared controlling the thickness of the diffuse interface, and $|\cdot|$ denotes the norm of a vector.

We consider the coupling energy density which is also called the elastic strain energy density, defining the coupling between diffusion and mechanics, in the form³⁸

$$\begin{aligned} \psi^{cp} &= \frac{1}{2} \varepsilon^e : \mathbb{C} : \varepsilon^e \\ &= G \left(\varepsilon^e : \varepsilon^e + \frac{\nu}{1-2\nu} (\text{tr } \varepsilon^e)^2 \right). \end{aligned} \quad [4]$$

Here \mathbb{C} is the elasticity tensor

$$\mathbb{C} = G(\delta_{ik} \delta_{jl} + \delta_{il} \delta_{jk}) + \frac{2G\nu}{1-2\nu} \delta_{ij} \delta_{kl}, \quad [5]$$

which is taken to be constant and isotropic. Accordingly, ν is the Poisson number, and $G = E/2(1 + \nu)$ is the shear modulus, where E is the Young's modulus.

The elastic strain ε^e is given by

$$\varepsilon^e = \varepsilon - \varepsilon^s, \quad [6]$$

where

$$\varepsilon^s = \frac{1}{3} \Omega (c - c_0) \mathbf{I} \quad [7]$$

is the stress-free strain induced by species insertion or extraction, and ε is the linear strain tensor

$$\varepsilon_{ij} = \frac{1}{2} (u_{i,j} + u_{j,i}) \quad [8]$$

with u_i being the displacement vector. Here, Ω is the partial molar volume, and c_0 is the initial species concentration.

The stress tensor can be derived from the free energy density,³⁸ which leads to the law of linear elasticity

$$\begin{aligned} \mathbf{T} &= \frac{\partial \psi(c, \text{grad } c, \varepsilon)}{\partial \varepsilon} \\ &= \mathbb{C} : \varepsilon^e. \end{aligned} \quad [9]$$

The driving force for diffusion is expressed as the gradient of the chemical potential. Based on the local dissipation inequality and the so-called local microforce balance,³⁸ the chemical potential is a superposition of three terms

$$\mu = \frac{\delta \Psi}{\delta c} = \frac{\partial \psi^{mwp}}{\partial c} - k_B T_{ref} N_A \lambda \text{div}(\text{grad } \bar{c}) + \mu^{cp}. \quad [10]$$

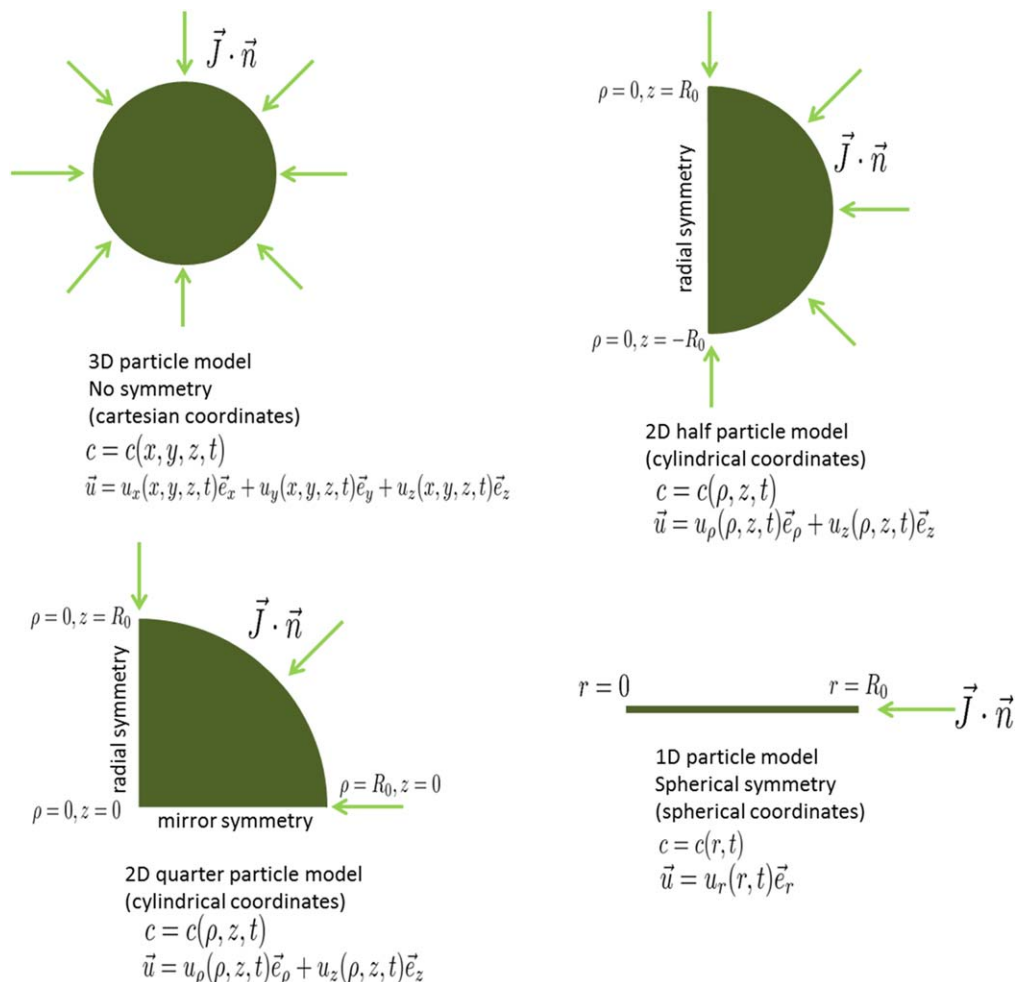


Figure 1. Different assumptions regarding the symmetries of the system states correspond to different particle models.

Here, μ^{cp} is the coupling chemical potential

$$\mu^{cp} = -\Omega T_H, \quad [11]$$

where $T_H = 1/3T_{ii}$ is the hydrostatic stress.

The constitutive equation for the mass flux can be expressed as the Onsager relation³⁸

$$\vec{J} = -\mathbf{M} \cdot \text{grad } \mu, \quad [12]$$

where the mobility tensor \mathbf{M} is non-negative definite. We choose an isotropic mobility according to

$$\mathbf{M}(c) = M(c)\mathbf{I} \quad [13]$$

with the function

$$M(c) = \frac{D_0 c (c_{\max} - c)}{k_B T_{\text{ref}} N_A c_{\max}}, \quad [14]$$

which is symmetric in the range between zero and maximum concentration and in which D_0 is the diffusion coefficient.

Finally, based on the balances of mass and momentum, respectively, we can obtain the field equations

$$\frac{\partial c}{\partial t} = \text{div} (M(c) \text{grad } \mu), \quad [15]$$

$$\text{div } \mathbf{T} = \vec{0}. \quad [16]$$

Combined with the constitutive equation introduced above, the field equation form a system of partial differential equation for concentration c and displacement vector \vec{u} , which need to be solved for

given initial and boundary conditions. This is a fourth-order nonlinear initial-boundary-value problem.

Model dimensionality.—We consider a spherical cathodic particle of radius R_0 . Such the spherically shaped particle is consistent with the experimental sample of NaFPO with a nearly spherical shape.⁴ For the purpose of achieving representative statements, we assume that it is sufficient to consider in a first step spherical particles. Because, in this way we neglect effects due to geometrical features specific to individual particle shapes. In order to avoid costly expensive 3D simulations, depending on whether symmetries regarding the unknown variables including the species concentration c and the displacement vector \vec{u} are assumed or not,⁴¹ a spherical particle with vanishing stress and isotropically applied species flux at its surface may be represented by different particle models, as illustrated in Fig. 1.

Under the assumption of spherical symmetry, the 3D problem is allowed to be replaced by an equivalent 1D problem using spherical coordinates, as sketched in Fig. 1. Due to the spherical symmetry, all fields are expressed as a function of the time t and the radial coordinate $0 \leq r \leq R_0$.

$$c = c(r, t), \quad [17]$$

$$\vec{u} = u_r(r, t)\vec{e}_r. \quad [18]$$

On the other hand, using the cylindrical coordinate system, it can be assumed that not only the particle geometry but also the unknown variables and the boundary conditions are symmetric under rotation around z -axis. As a result, under the aforementioned radial

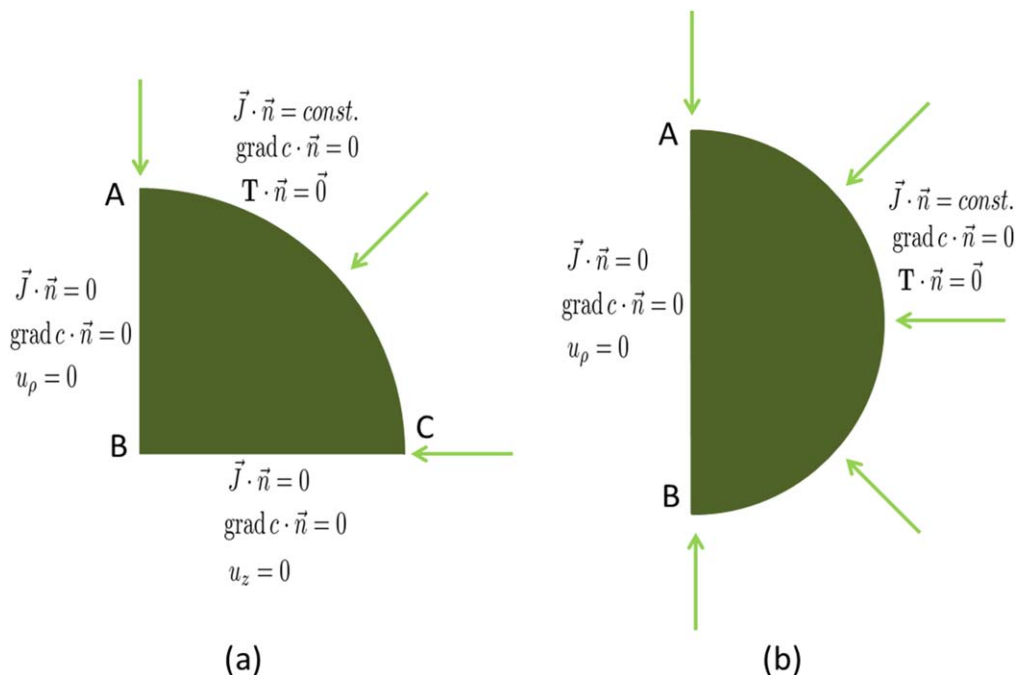


Figure 2. Boundary conditions for 2D particle models: (a) 2D quarter particle model; (b) 2D half particle model.

symmetry, the 3D problem can be replaced by a 2D problem. Depending on whether the mirror symmetry is assumed or not, the 2D particle model can be represented by the 2D quarter particle model or the 2D half particle model, respectively, as sketched in Fig. 1. It should be noticed that the 2D particle model also can be used to represent ellipsoidal particles of two equal semi-axis. In the 2D particle model, all fields are assumed to satisfy

$$c = c(\rho, z, t), \quad [19]$$

$$\vec{u} = u_\rho(\rho, z, t)\vec{e}_\rho + u_z(\rho, z, t)\vec{e}_z. \quad [20]$$

Boundary conditions.—Here, we just focus on the boundary conditions for 2D particle models. With regard to the boundary conditions for the spherically symmetry boundary value problem, please see our recent work.⁴²

The boundary conditions are sketched in Fig. 2. For the diffusion, a spatially independent mass flux at the surface is chosen as

$$\vec{J} \cdot \vec{n} = \begin{cases} -\frac{C c_{\max} R_0}{3600 \cdot 3} & \text{for } c \leq c_{\max}, \\ 0 & \text{for } c = c_{\max} \end{cases}, \quad [21]$$

where \vec{n} refers to the outgoing unit vector normal to the particle surface. Here C is the C -rate, and $C = 1$ means that the amount of species of a fully charged particle would flow into the particle within 1 h. Once the maximum concentration c_{\max} is reached anywhere at the surface, the mass flux will be stopped.

A vanishing flux condition

$$\vec{J} \cdot \vec{n} = 0, \quad [22]$$

is imposed on the boundaries AB and BC for the 2D quarter particle model, and the interior boundary AB for the 2D half particle model.

Also, neglecting surface wetting, the “natural” boundary condition²³

$$\text{grad } c \cdot \vec{n} = 0 \quad [23]$$

is imposed on all boundaries. When the interface between two phases intersects the particle surface, Eq. 23 enforces that it is perpendicular to the surface.^{30,32}

For the mechanical part, the particle is assumed to be stress free at the surface:

$$\mathbf{T} \cdot \vec{n} = \vec{0}. \quad [24]$$

For the 2D quarter particle model, the boundaries AB and BC are constrained to have no radial and vertical displacements, respectively.³⁵

$$u_\rho(\rho = 0, z) = 0, \quad [25]$$

$$u_z(\rho, z = 0) = 0. \quad [26]$$

Similarly, the interior boundary AB of the 2D half particle model is constrained to have no radial displacement.

Material parameters.—We choose a typical particle radius of $R_0 = 500$ nm. The material parameters for the two cathode materials NaFPO and LiFPO are summarized in Table I. For the detailed determination of the material parameters for NaFPO, for example, α_1 , α_2 , and λ , all of which are the key parameters in the phase-field model, see Ref. 24. Here, we just focus on the two-phase region of NaFPO ($0 < x < 2/3$) in our simulations. The anisotropy of mobility will prefer certain directions of transport, but not influence the final system state which is thermodynamically determined.³⁶ Indeed, Tang et al.³⁶ also have pointed out that the cases without and with considering the anisotropy of mobility will eventually exhibit the same equilibrium states that are the most energetically favorable, although the relaxation may be extremely slow for the anisotropic case. Consequently, it is expected that the anisotropic property makes no significant effect on the quasiequilibrium states of the system that are investigated in our simulations. To simplify the current work, we therefore do not take the anisotropy into account in our model. The detailed discussion of anisotropy of the crystal, including the anisotropic diffusion, the anisotropic gradient energy, the anisotropic deformation, and the anisotropic geometry, is beyond the scope of this work. One can refer to these reports^{30–34,43} for more information.

The resulting set of equations has been implemented in the finite-element, multiphysics framework MOOSE for solution. MOOSE allows mesh adaptivity and time step adaptivity, as well as parallelization. Using these numerical capabilities, the 2D simulation

Table I. The material parameters for the two cathode materials.

Parameter	NaFPO	LiFPO
α_1	5 (Ref. 24)	4.5 (Ref. 32)
α_2	-15 (Ref. 24)	-9 (Ref. 32)
λ	1.8×10^{-17} (m ²) (Ref. 24)	8.8×10^{-18} (m ²) (Ref. 32)
D_0	1×10^{-15} (m ² s ⁻¹) (Ref. 24)	1×10^{-14} (m ² s ⁻¹) (Ref. 44)
c_{\max}	2.1×10^4 (mol m ⁻³) (Ref. 24)	2.29×10^4 (mol m ⁻³) (Ref. 45)
Ω	8.8×10^{-6} (m ³ mol ⁻¹) (Ref. 24)	2.9×10^{-6} (m ³ mol ⁻¹) (Ref. 40)
E_0	120 (GPa) (Ref. 24)	124.5 (GPa) (Ref. 46)
ν	0.25 (Ref. 46)	0.25 (Ref. 46)

of time dependent insertion processes in electrode particles including the coupling to mechanics is achieved. In particular, the mesh adaptivity effectively handles the numerical difficulty that the moving interface between two phases with its strong gradients requires adequate resolution. Besides accuracy, the cost of the simulation also should be taken into account meaning that the mesh should be coarsened in regions of weak gradients. Simulations are performed on a high performance Linux computer cluster. In order to validate the MOOSE implementation, we also implemented the 1D Cahn–Hilliard model in COMSOL Multiphysics®.

Results and Discussion

In this section, we will consider the quasistatic insertion of species into cathodic particles at $C=0.001$. With this C -rate, we study the behavior for dynamic, i.e. continuous insertion very close to a sequence of equilibrium states. In this way, the system is allowed to move along a path of relaxed quasiequilibrium states. It should be noticed that, in the absence of mechanics, $C=0.0001$ is used in the simulations for NaFPO to reach the quasiequilibrium state due to the relatively lower diffusion coefficient of Na-ions in NaFPO, as shown in Table I. In the Figures, the average concentration c_{avg} , also called “state of charge” (SOC) is $c_{\text{avg}} = \int_{\mathcal{B}} \bar{c} dV/V$. Furthermore, the dimensionless free energy density is introduced as $\bar{\psi} = \psi/(k_B T_{\text{ref}} N_A c_{\text{max}})$, and $\bar{\Psi}_{\text{avg}} = \int_{\mathcal{B}} \bar{\psi} dV/V$ is the dimensionless average system free energy, see also Eq. 1.

Validation of MOOSE implementation.—We first compare the simulation results between MOOSE and COMSOL, based on the 1D particle model for the cathode material LiFPO. Figure 3a shows the comparison of the concentration plots from the two simulation tools at a stage of average concentration of $c_{\text{avg}} = 0.5$, including the pure and mechanically coupled diffusion cases. We find that the

phase-segregated concentration field from MOOSE matches that from COMSOL, no matter in the pure or mechanically coupled diffusion case. The concentration field exhibits a “core–shell” structure of spherical symmetry. Two different phases can be recognized in the particle, namely the species-poor phase in the inner core and the species-rich phase at the the outer shell of the particle. A smooth but very narrow interface with concentration changing rapidly but continuously separates them. In addition, a shrinking miscibility gap between two phases in the mechanically coupled diffusion case is observed due to the counteraction to phase segregation by the elastic strain energy. Also, the plots of hydrostatic stress from the two simulation tools match each other, as shown in Fig. 3b. Therefore, the MOOSE implementation is validated by the above agreement with the COMSOL solutions.

Influences of the model dimensionality and mirror symmetry.

—In order to investigate the influences of the model dimensionality and mirror symmetry, we first exclude the effect of mechanics. Under the quasistatic loading conditions considered here, the system will be close to equilibrium. When relaxing toward equilibrium without any loading, the system will follow a path of decreasing system free energy. Therefore, we will compare the system free energy in the different particle models.

In Fig. 4, as compared to the state of spherical symmetry obtained using the 1D particle model, the phase-segregated concentration field of LiFPO obtained using the 2D quarter particle model at $c_{\text{avg}} = 0.5$, is not of spherical symmetry, i.e. it does not show the same symmetry as the particle geometry any more. Instead, the phase boundary in the 2D quarter particle model extends from surface to surface such that its proportion in the particle becomes as low as possible. Indeed, such asymmetric state possesses a lower free energy than that obtained using the 1D particle model. Now we study the influence of the mirror symmetry in the particle models. As

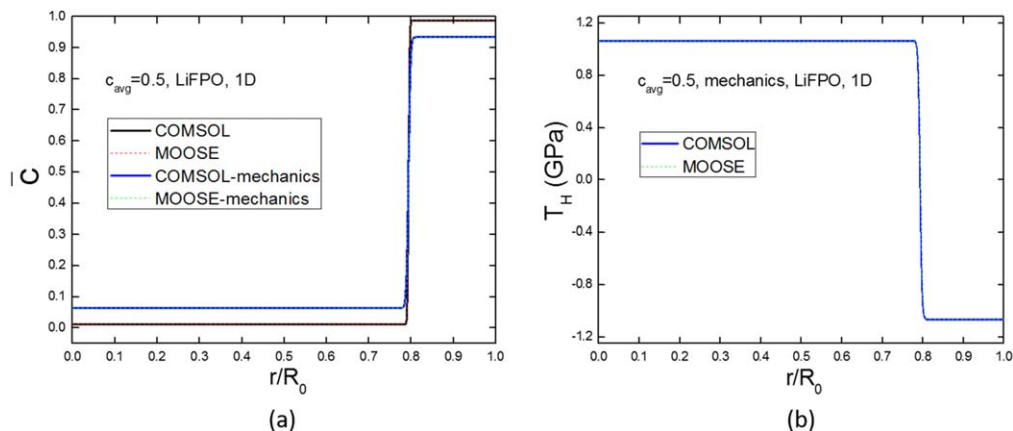


Figure 3. (a) Normalized concentration \bar{c} vs normalized radial coordinate r/R_0 at $c_{\text{avg}} = 0.5$ during insertion for the pure and mechanically coupled diffusion cases of LiFPO; (b) hydrostatic stress T_H vs normalized radial coordinate r/R_0 at $c_{\text{avg}} = 0.5$ during insertion for LiFPO: comparison of the simulation results between MOOSE and COMSOL.

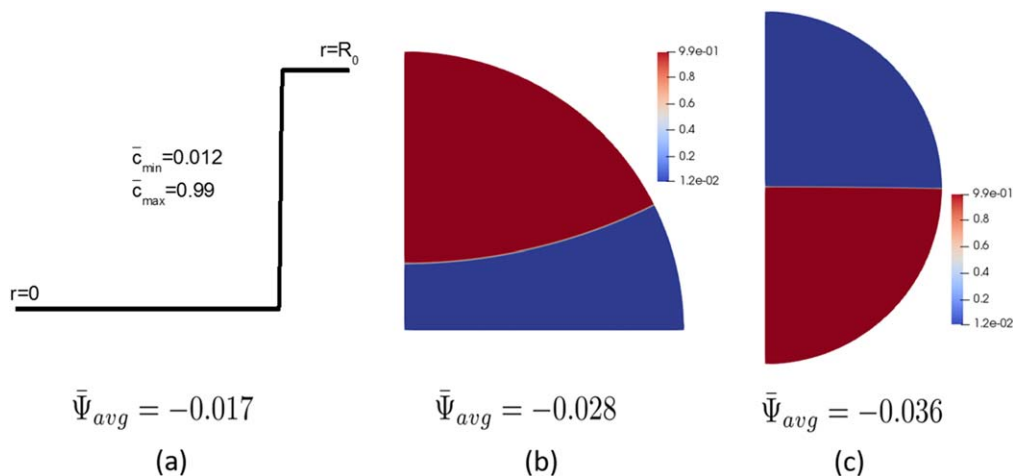


Figure 4. Lithium concentration profiles and related normalized average system free energy of LiFPO at $c_{avg} = 0.5$ during insertion: (a) 1D particle model, (b) 2D quarter particle model; (c) 2D half particle model.

shown in Fig. 4c, compared to the asymmetric state obtained using the 2D quarter particle model, the phase-segregated concentration field obtained using the 2D half particle model at $c_{avg} = 0.5$ exhibits a phase boundary going across the particle equator such that its proportion in the particle is further minimized. As expected, such asymmetric state possesses an even lower system free energy than that obtained using the 2D quarter particle model. Therefore, the mirror symmetry of the system state can be destroyed in order to minimize the system free energy.

Microstructure evolution.—In this part, we study the microstructure evolution of NaFPO during the process of insertion, and compare it with that of LiFPO. Here, we still exclude the effect of mechanics. As discussed in the previous section, the mirror symmetry of phase segregation can be destroyed, thus we make use of the 2D half particle model.

Figure 5 shows the system free energy evolution of the two cathode materials NaFPO and LiFPO during the process of insertion by the solid lines, and the corresponding microstructure evolution for each material is shown in Fig. 6. For comparison purposes, both, the dimensionless multiwell potential vs the normalized concentration and the plots of the system free energy evolution obtained using the 1D particle model are also entered in Fig. 5. $\bar{\psi}^{mwp}$ exhibits a doublewell structure, such that two different relative minima occur, characterizing two phases related to the two different solubility

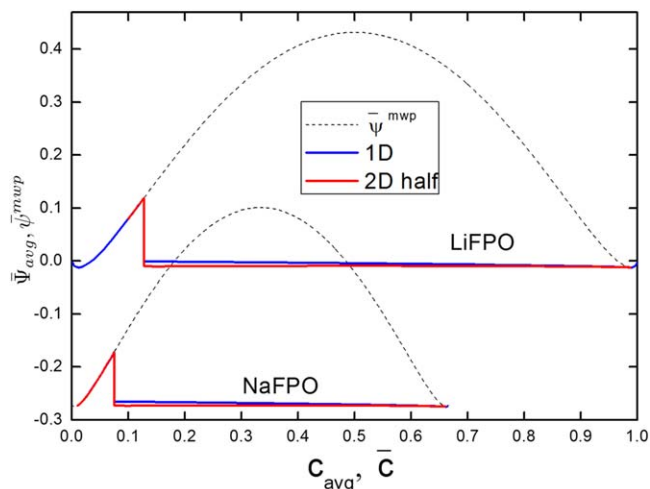


Figure 5. Normalized average system free energy $\bar{\Psi}_{avg}$ and normalized homogeneous free energy density $\bar{\psi}^{mwp}$ as function of c_{avg} and \bar{c} , respectively, for the pure diffusion cases of NaFPO and LiFPO.

limits. The Maxwell construction, which connects the neighborhoods of the two minima by a common tangent, represents the volume fractions of the two phases in a phase segregated state. The two ranges between the respective tangent points of the Maxwell construction and the neighboring inflection points are the “nucleation zones”, and phase segregation is initiated upon sufficient disturbance of the system. In the inner zone of concavity between the two points of inflection, which is called the “spinodal decomposition zone”, homogeneous species concentration states are unstable and phase segregation is initiated in any case. Solid lines on the dimensionless multiwell potential curve correspond to homogeneous states whereas solid lines nearby the path of the Maxwell construction correspond to phase segregated states. We find that the system free energy at the phase-segregated states obtained using the 2D half particle model is lower than that obtained using the shrinking-core model for the two materials, see Fig. 5.

At the beginning of insertion, there is a homogeneous state for the two cathode materials, as shown in Fig. 6. Phase segregation is not initiated until c_{avg} reaches the respective “spinodal decomposition zone” of the dimensionless multiwell potential. It is found that, a species-rich island is initiated around the “pole” region, and more species-rich islands quickly form at the particle surface, when c_{avg} approaches 7.5% for NaFPO, which is earlier than 12.7% for LiFPO. Correspondingly, the respective system free energy undergoes a rapid dropping process at the beginning of phase segregation, see Fig. 5. Two different phases $FePO_4$ and $Na_{2/3}FePO_4$ are recognized for NaFPO, and its miscibility gap is about 2/3 of that of LiFPO. As time goes on, the number of species-rich islands in NaFPO decreases in order to minimize the proportion of interfaces. Due to the very low insertion rate, this is merely a process of time dependent relaxation of which the time constant is controlled by the diffusion constant. When c_{avg} approaches 9.37% for NaFPO, there exists a sole species-rich island occupying one of the “pole” regions, see the fifth column of Fig. 6a, which is also earlier than 14.17% for LiFPO. From now on, similar to LiFPO, NaFPO exhibits the dynamics of single wave propagation: the single species-rich island gradually expands along z -direction, and the phase boundary always goes all across the particle. Actually, as shown in Fig. 5, the single wave propagation dynamics is more energetically favorable than the shrinking-core dynamics. Such single wave propagation obtained from our isotropic model is close to the experimental observations for LiFPO.^{25–28} This finding is consistent with our assumption that the anisotropy of the transport properties has no significant effect on the final quasiequilibrium states of the system. It should be noticed that the above single wave propagation phenomenon is limited to particles of sufficient size. For smaller ones, the miscibility gap shrinks and even gets totally suppressed.^{32,36,42}

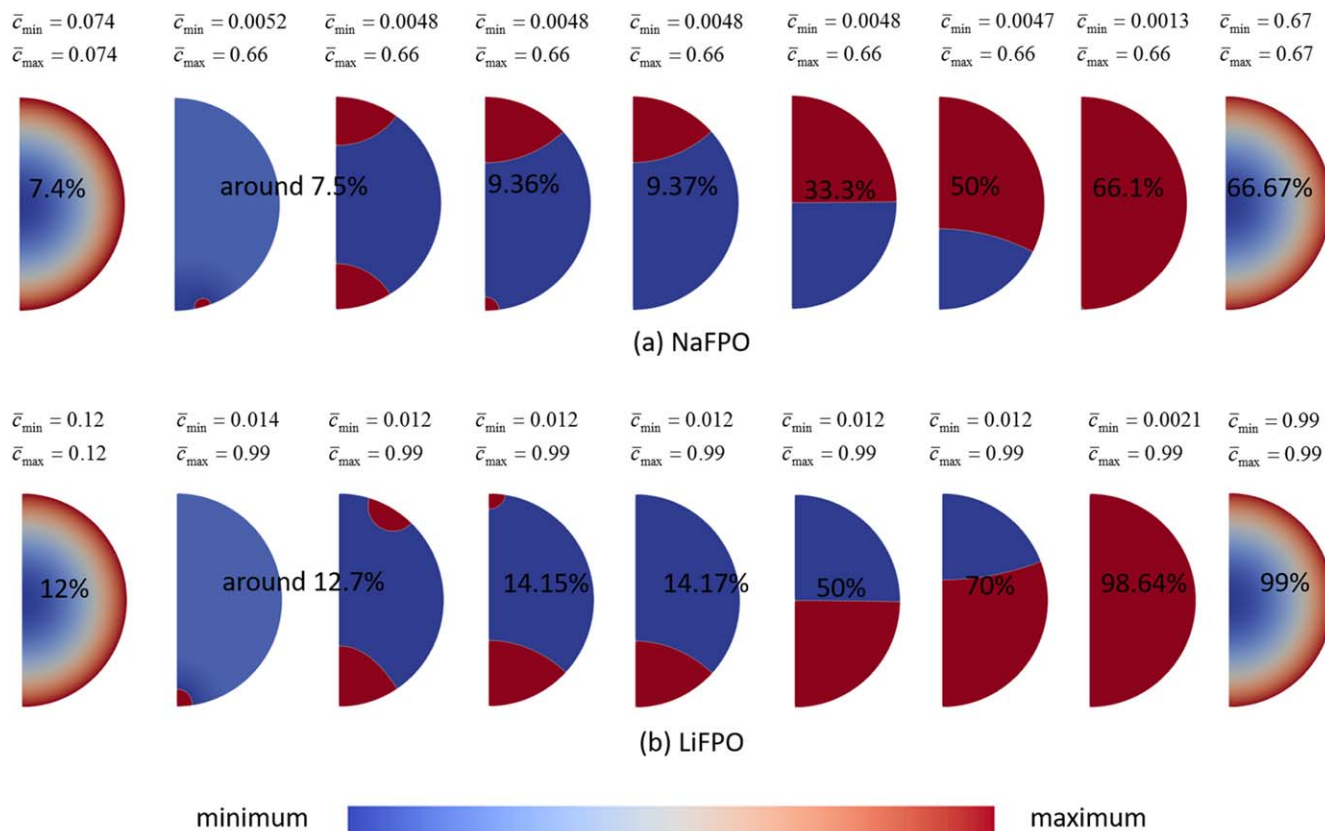


Figure 6. Microstructure evolution as function of c_{avg} for NaFPO and LiFPO: (a) NaFPO; (b) LiFPO.

It is interesting to see that, due to the interface minimization, the interface of each material changes from the convex shape to the concave shape with an intermediate shape of plane circularity at the center of the combined nucleation and spinodal zone. For example, the plane circular interface is achieved at $c_{avg} = 33.3\%$ for NaFPO but $c_{avg} = 50\%$ for LiFPO. Actually, during the single wave propagation process, the system is very close to a sequence of equilibrium states. This is well illustrated by a “hold time” simulation in which the applied flux is terminated during the single wave propagation process, and phase evolution during the “hold time” is monitored. It is found that the concentration field during the relaxation time is almost unaltered (we do not show this result here). When c_{avg} grows up to 66.1% for NaFPO, the intermediate phase $Na_{2/3}FePO_4$ will occupy all of the particle. However, LiFPO still exhibits phase segregation until at the end of the insertion process.

Influence of the elastic strain energy.—What is the influence of the elastic strain energy on the microstructure evolution? Figure 7 shows the system free energy evolution of two cathode materials in the mechanically coupled case during the process of insertion. Furthermore, the evolution of the microstructure and the corresponding hydrostatic stress for each material are shown in Figs. 8–9, respectively. For comparison purpose, both, the system free energy obtained using the mechanically coupled 1D particle model and that obtained using the 2D particle half model for the pure diffusion are also entered in Fig. 7. For NaFPO, in the presence of mechanics, the related system free energy obtained using the 1D particle model follows completely the dimensionless multiwell potential even in the nucleation and spinodal ranges of average concentration. This means that phase segregation is completely suppressed. Although phase segregation of LiFPO still occurs in the mechanically coupled 1D particle model, the system free energy at the phase segregated states is higher than that obtained using the mechanically coupled 2D half

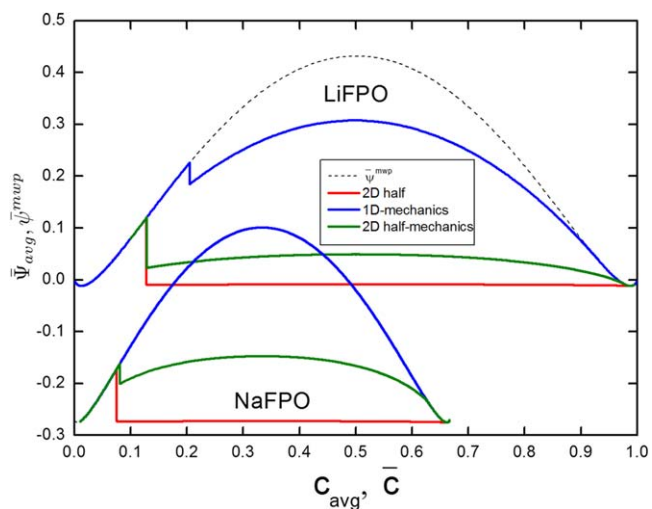


Figure 7. Normalized average system free energy $\bar{\Psi}_{avg}$ and normalized homogeneous free energy density $\bar{\Psi}^{mwp}$ as function of c_{avg} and \bar{c} , respectively, for NaFPO and LiFPO.

particle model. Therefore, in the presence of mechanics, the classical “core–shell” structure is extremely energetically unfavorable.

We can find that in Figs. 8–9, when considering mechanics, the onset of phase segregation is postponed for each material, see the second column of each Figure. Once phase segregation is initiated, c_{avg} approaching 8.1%, NaFPO immediately enters the single wave propagation process, which is earlier than 12.88% for LiFPO. When mechanics is accounted for, the interface thickness is widened due to the suppressing effect of the coupling energy, which is more

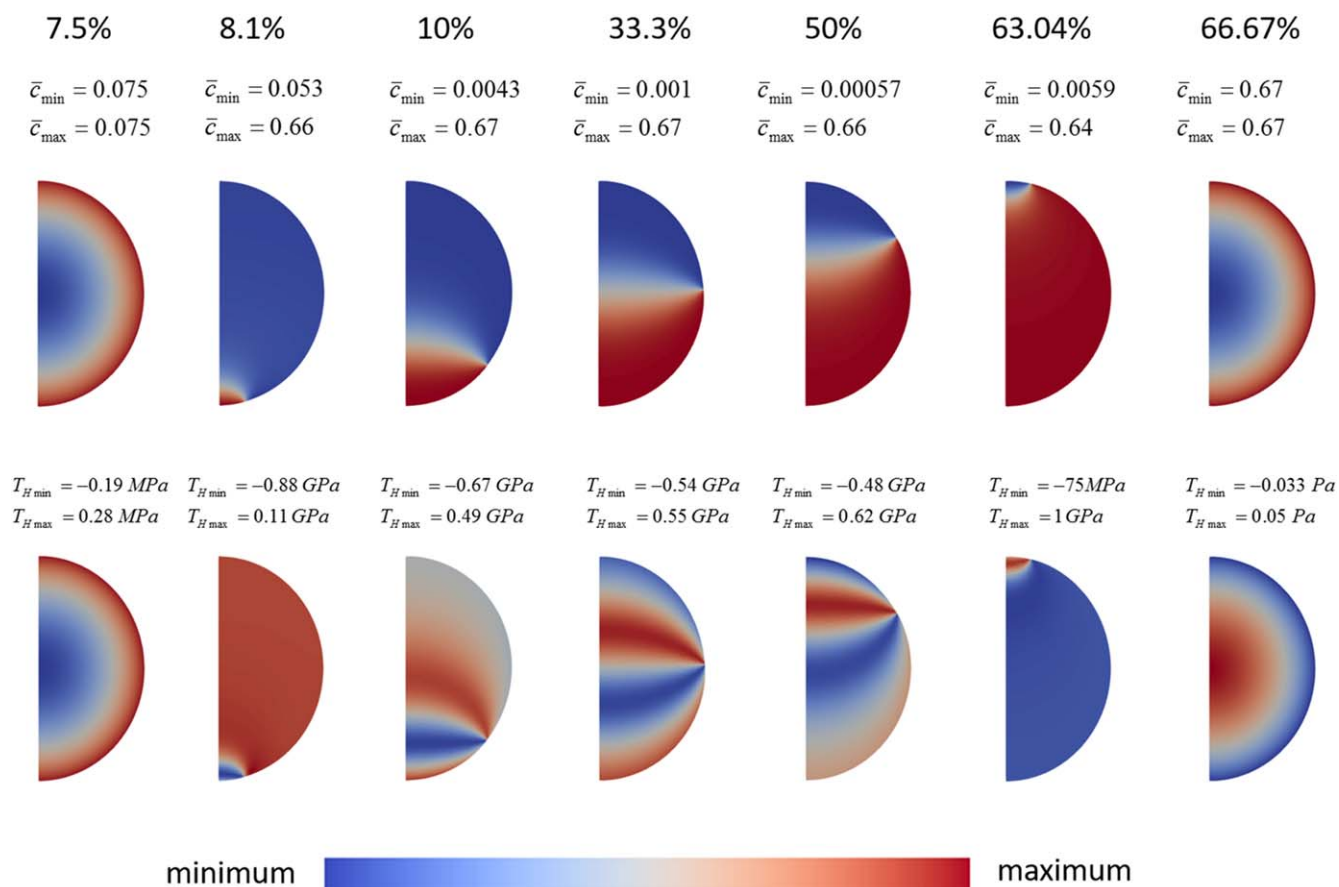


Figure 8. Evolution of the microstructure and the corresponding hydrostatic stress as function of c_{avg} for NaFPO.

pronounced for NaFPO. It should be mentioned that the phase-segregated state of LiFPO, for example at $c_{avg} = 50\%$, matches the simulation result from a fully 3D mechanically coupled phase-field model.³⁶ Interestingly, in contrast to the constant stresses in each phase from the classical “core-shell” structure (see Fig. 3), both, tensile and compressive stresses are present in each phase for the two materials. Indeed, along the moving interface direction, the stress in each phase changes gradually from tensile stresses to compressive stresses. It means that there exists the tensile stresses at the particle surface occupied by the species-rich phase but there are compressive stresses at the particle surface occupied by the species-poor phase. In the presence of surface defects, the particle surface occupied by the species-rich phase is more prone to cracking during insertion.

According to Eq. 11, the gradient of hydrostatic stress in each phase makes a mechanical contribution to the driving force for diffusion along z -direction. As a result, a concentration inhomogeneity in each phase is evoked, as shown in Fig. 10. Figure 10 shows the concentration at the center of the combined nucleation and spinodal zone ($c_{avg} = 0.333$ for NaFPO, and $c_{avg} = 0.5$ for LiFPO) plotted along the rotational axis AB for each material. For comparison purposes, the concentration plots in the absence of mechanics are also entered. We can see that the concentration gradient in each phase is steeper for NaFPO. The existence of a concentration gradient requires a reconsideration of the definition of the solubility limit in the mechanically coupled cases. Here, in analogy with Wagemaker et al.⁴⁷ we also introduce the average solubility limit to represent the composition in each phase, which is shown as solid horizontal line in Fig. 10. According to Wagemaker et al.,⁴⁷ the average solubility limit is also the right quantity for comparison with experimental measurements in which diffraction probes the average species occupancy.

The experimentally measured solubility limits of NaFPO⁶ and LiFPO⁴⁷ are shown as dash horizontal lines in Fig. 10. We find the calculated low and high average solubility limits $Na_{0.08}FePO_4$ and $Na_{0.6}FePO_4$ as well as $Li_{0.03}FePO_4$ and $Li_{0.98}FePO_4$ when mechanics is considered, for NaFPO and LiFPO, respectively. Our calculated average solubility limits in the presence of mechanics match the experimental values for NaFPO and LiFPO. What is more, in the presence of mechanics, there exists a reduced miscibility gap for each material, as shown in Fig. 10. In contrast to LiFPO, the miscibility gap of NaFPO is significantly reduced. This means that the elastic strain energy has a stronger impact on the miscibility gap in NaFPO compared to LiFPO.

Now we compare the hydrostatic stress at the center of the combined nucleation and spinodal zone for the two cathode materials plotted along the rotational axis AB, as shown in Fig. 11. Compared to LiFPO, the stress magnitudes at the interface are smaller in a NaFPO particle due to the relatively widened interface. Although the miscibility gap of NaFPO is smaller than that of LiFPO, both, the tensile stress magnitudes in the “south pole” region and the compressive stress magnitudes in the “north pole” region of NaFPO are larger, and they even are at the same level as the stresses induced at the interface of this material. This is due to the larger expansion, i.e. partial molar volume, during phase segregation for NaFPO, which is related to a larger cation radius of sodium. Actually, the stress magnitudes at the particle surface are larger in a NaFPO particle than these in a LiFPO particle, see Figs. 8–9. Therefore, it is expected that the particle surface of NaFPO is more prone to damage than that of LiFPO. Our work suggests that the NaFPO particles can be designed through particle coatings to prevent particle cracking for improving mechanical stability and consequently better battery performance.

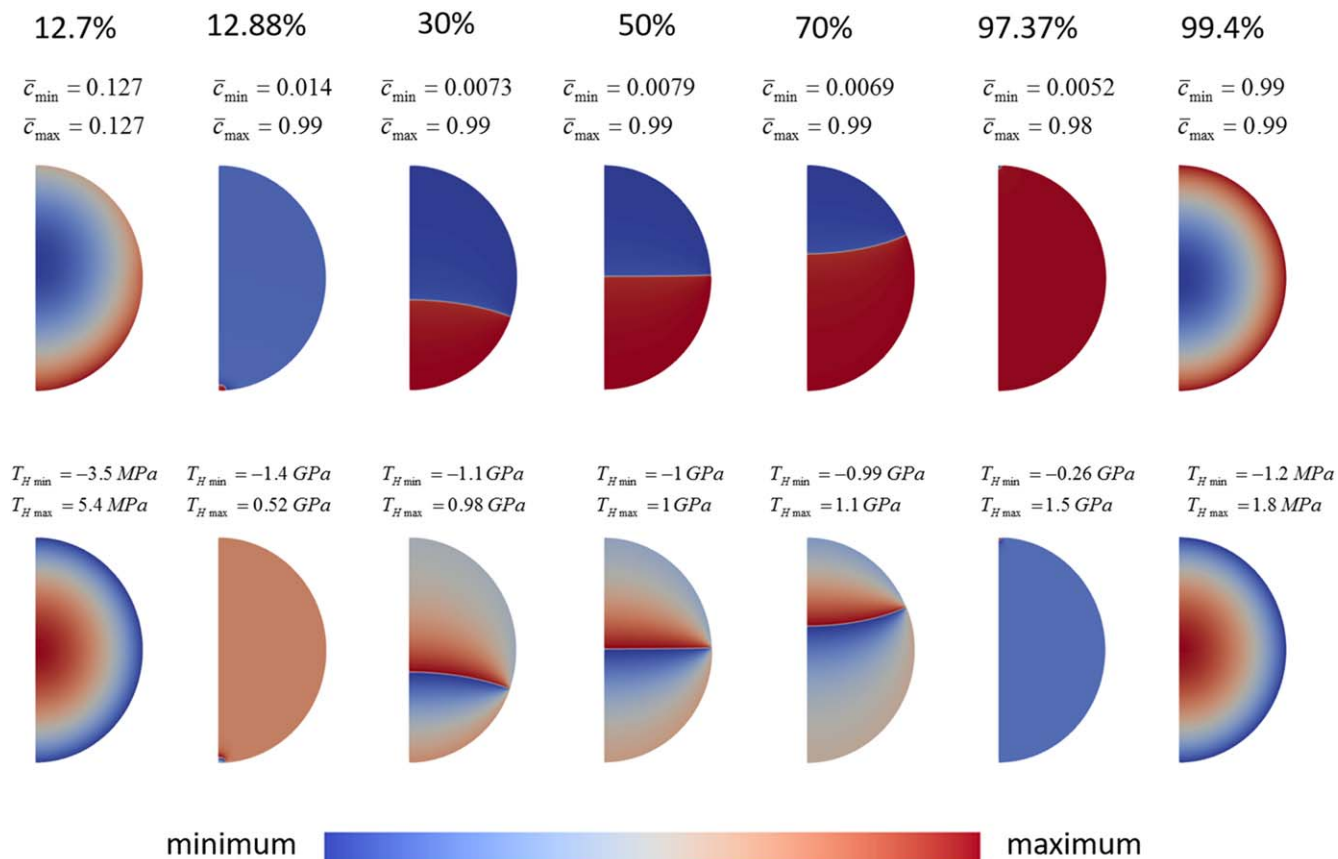


Figure 9. Evolution of the microstructure and the corresponding hydrostatic stress as function of c_{avg} for LiFPO.

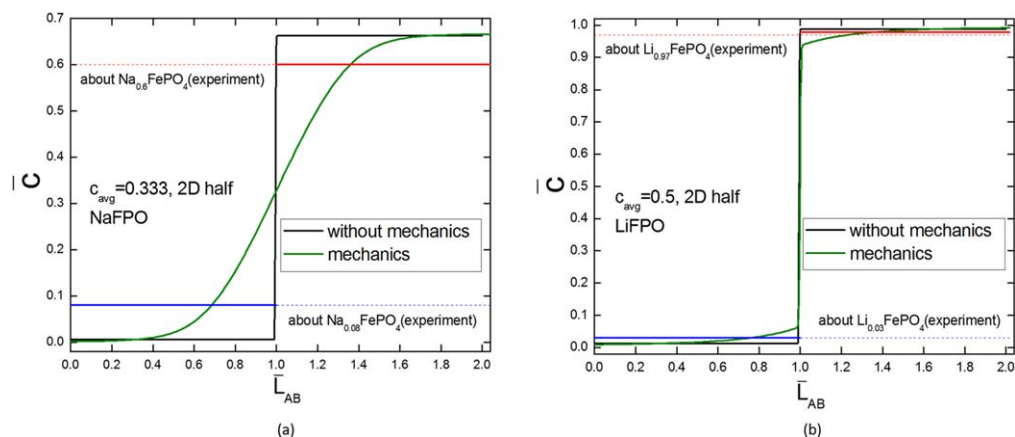


Figure 10. Normalized concentration and calculated average solubility limits at the center of the combined nucleation and spinodal zone ($c_{avg} = 0.333$ for NaFPO, and $c_{avg} = 0.5$ for LiFPO) for the two cathode materials plotted along the rotational axis AB. The red straight line represents the calculated high average solubility limit, and the blue straight line represents the calculated low average solubility limit. The dashed horizontal lines represent the experimental results for NaFPO⁶ and LiFPO,⁴⁷ respectively: (a) NaFPO; (b) LiFPO.

Conclusions

By means of the Cahn–Hilliard theory with the coupling to mechanics, the microstructure evolution of phase segregation during the time dependent insertion process has been investigated for the cathode material NaFPO of NIBs. A direct comparison between NaFPO and LiFPO is made in terms of the microstructure evolution and the stress evolution. We implemented the fourth-order nonlinear initial-boundary-value problem of the model in the finite-element, multiphysics framework MOOSE to solve the 2D problem, using mesh adaptivity and time step adaptivity, as well as parallelization.

The dynamics of single wave propagation is obtained for NaFPO, and both, the classical “core–shell” structure and the mirror symmetry of phase segregation may be destroyed in order to obtain states of lower free energy. The interface morphology that goes across the particle dynamically changes in order to minimize its proportion.

When mechanics is accounted for, phase segregation of NaFPO is completely suppressed in the shrinking-core model. In the presence of mechanics, single wave propagation immediately occurs once phase segregation is initiated during the quasistatic insertion, and the interface is widened, which is more pronounced for NaFPO. The elastic strain energy plays a more significant role on the miscibility gap in this

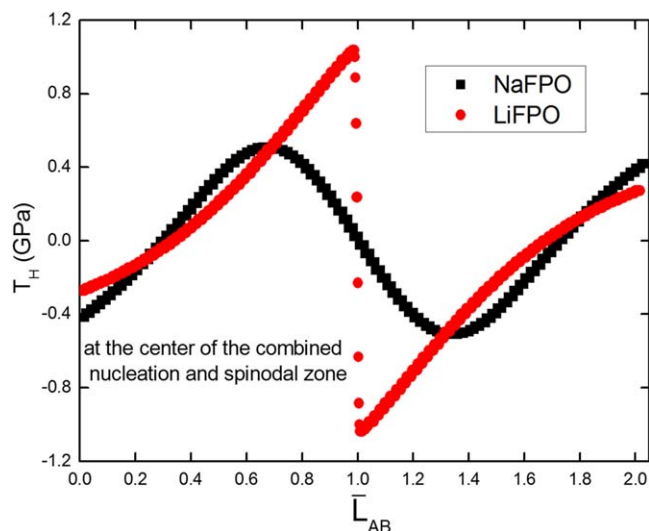


Figure 11. Normalized hydrostatic stress at the center of the combined nucleation and spinodal zone for NaFPO and LiFPO plotted along the rotational axis AB.

material compared to LiFPO. In contrast to the constant stresses in each phase obtained from shrinking-core dynamics, both, tensile and compressive stresses coexist in each phase. Because of this, the particle surface occupied by the species-rich phase is more prone to cracking due to the tensile stresses in this region. The gradient of hydrostatic stress in each phase induces a more developed concentration inhomogeneity for NaFPO. In comparison to LiFPO, the stress magnitudes at the interface are smaller in a NaFPO particle due to the relatively widened interface. Although the miscibility gap of NaFPO is smaller than that of LiFPO, the stress magnitudes at the particle surface are larger in a NaFPO particle, which makes it less mechanically reliable. In view of this it can be expected that coating of NaFPO particles may prevent particle cracking for better battery performance.

In this work, we focus on the 2D half particle model, which goes beyond considering the mirror symmetry of the particle. However, for spherical LiFPO particles with the radius of 40 nm, Welland et al.³⁶ find that $Li_{0.8}FePO_4$ shows no symmetric microstructure in their fully 3D simulations. The fully 3D mechanically coupled anisotropic phase-field model of NaFPO will be subject of future work. In addition, while we concentrate on the behavior of individual intercalation particles, it has to be mentioned that the intercalation particles are usually embedded in a porous binder matrix. Shpigel et al.⁴⁸ investigated the particle-binder interactions in NaFPO/binder electrodes by in situ acoustic diagnostics. They reported that there is a clear difference in the microstructure evolution of composite NaFPO and LiFPO electrodes using rigid binders. The large NaFPO expansion leads to the destruction of a rigid binder, and as a result, the mechanical connection between particles is lost. Thus, a rigid binder is not suitable to accommodate the large expansion of NaFPO particles. As shown in their work, soft binders allow the free expansion of the intercalation particles of NaFPO, thus accommodating the large strain. It can be expected that soft binders may not significantly influence the microstructure evolution in NaFPO particles. Therefore, the particle-binder interactions may play a significant role in microstructure evolution of the composite electrodes, especially for rigid binders, in respect to the occurrence of cracks either in the intercalation particles or the surrounding binder network. Investigating the effect of the polymeric binders on the microstructure evolution in composite NaFPO electrodes will also be subject of future work.

Acknowledgments

The author Tao Zhang is supported by China Scholarship Council (CSC). This work contributes to the research performed at CELEST

(Center for Electrochemical Energy Storage Ulm-Karlsruhe) and was funded by the German Research Foundation (DFG) under Project ID 390874152 (POLiS Cluster of Excellence). We would like to thank Dr. Karthikeyan Chockalingam for very instructive discussions about the MOOSE implementation. The authors acknowledge support by the state of Baden-Württemberg through bwHPC.

References

1. J. Kim, D.-H. Seo, H. Kim, I. Park, J.-K. Yoo, S.-K. Jung, Y.-U. Park, W. A. Goddard III, and K. Kang, *Energy Environ. Sci.*, **8**, 540 (2015).
2. V. Palomares, P. Serras, I. Villaluenga, K. B. Hueso, J. Carretero-González, and T. Rojo, *Energy Environ. Sci.*, **5**, 5884 (2012).
3. M. Casas-Cabanas, V. V. Roddatis, D. Saurel, P. Kubiak, J. Carretero-González, V. Palomares, P. Serras, and T. Rojo, *J. Mater. Chem.*, **22**, 17421 (2012).
4. Y. J. Zhu, Y. H. Xu, Y. H. Liu, C. Luo, and C. S. Wang, *Nanoscale*, **5**, 780 (2013).
5. J. C. Lu, S. C. Chung, S.-i. Nishimura, and A. Yamada, *Chem. Mater.*, **25**, 4557 (2013).
6. K. Xiang et al., *Nano Lett.*, **17**, 1696 (2017).
7. J. Christensen and J. Newman, *J. Solid State Electr.*, **10**, 293 (2006).
8. M. Klinsmann, D. Rosato, M. Kamlah, and R. M. McMeeking, *J. Electrochem. Soc.*, **163**, A102 (2016).
9. L. R. De Jesus, Y. Zhao, G. A. Horrocks, J. L. Andrews, P. Stein, B.-X. Xu, and S. Banerjee, *J. Mater. Chem. A*, **5**, 20141 (2017).
10. R. Xu, H. Sun, L. S. de Vasconcelos, and K. Zhao, *J. Electrochem. Soc.*, **164**, A3333 (2017).
11. R. Xu and K. Zhao, *J. Mech. Phys. Solids*, **121**, 258 (2018).
12. D. Chen, D. Kramer, and R. Mönig, *Electrochim. Acta*, **259**, 939 (2018).
13. K. Zhao, M. Pharr, Q. Wan, W. L. Wang, E. Kaxiras, J. J. Vlassak, and Z. Suo, *J. Electrochem. Soc.*, **159**, A238 (2012).
14. Z. Guo, T. Zhang, H. Hu, Y. Song, and J. Zhang, *J. Appl. Mech.*, **81**, 031013 (2014).
15. C. V. Di Leo, E. Rejovitzky, and L. Anand, *Int. J. Solids Struct.*, **67**, 283 (2015).
16. M. Klinsmann, D. Rosato, M. Kamlah, and R. M. McMeeking, *J. Mech. Phys. Solids*, **92**, 313 (2016).
17. M. Ganser, F. E. Hildebrand, M. Kamlah, and R. M. McMeeking, *J. Mech. Phys. Solids*, **125**, 681 (2019).
18. Y. Zhao, P. Stein, Y. Bai, M. Al-Siraj, Y. Yang, and B.-X. Xu, *J. Power Sources*, **413**, 259 (2019).
19. R. Xu, Y. Yang, F. Yin, P. Liu, P. Cloetens, Y. Liu, F. Lin, and K. Zhao, *J. Mech. Phys. Solids*, **129**, 160 (2019).
20. J. W. Cahn and J. E. Hilliard, *J. Chem. Phys.*, **28**, 258 (1958).
21. T. Zhang and M. Kamlah, *Continuum Mech. Thermodyn.*, **30**, 553 (2018).
22. M. Huttin and M. Kamlah, *Appl. Phys. Lett.*, **101**, 133902 (2012).
23. Y. Zeng and M. Z. Bazant, *SIAM J. Appl. Math.*, **74**, 980 (2014).
24. T. Zhang and M. Kamlah, *J. Electrochem. Soc.*, **165**, A1997 (2018).
25. G. Chen, X. Song, and T. J. Richardson, *Electrochem. Solid-State Lett.*, **9**, A295 (2006).
26. L. Laffont, C. Delacourt, P. Gibot, M. Y. Wu, P. Kooyman, C. Masquelier, and J. M. Tarascon, *Chem. Mater.*, **18**, 5520 (2006).
27. C. Delmas, M. Maccario, L. Croguennec, F. Le Cras, and F. Weill, *Nat. Mater.*, **7**, 665 (2008).
28. C. Ramana, A. Mauger, F. Gendron, C. Julien, and K. Zaghib, *J. Power Sources*, **187**, 555 (2009).
29. J. Santoki, D. Schneider, M. Selzer, F. Wang, M. Kamlah, and B. Nestler, *Model. Simul. Mater. Sci. Eng.*, **26**, 065013 (2018).
30. Y. Zhao, P. Stein, and B.-X. Xu, *Comput. Meth. Appl. M.*, **297**, 325 (2015).
31. G. K. Singh, G. Ceder, and M. Z. Bazant, *Electrochim. Acta*, **53**, 7599 (2008).
32. D. A. Cogswell and M. Z. Bazant, *ACS Nano*, **6**, 2215 (2012).
33. D. A. Cogswell and M. Z. Bazant, *Nano Lett.*, **13**, 3036 (2013).
34. N. Nadkarni, T. Zhou, D. Fraggedakis, T. Gao, and M. Z. Bazant, *Adv. Funct. Mater.*, **29**, 1902821 (2019).
35. C. V. D. Leo, E. Rejovitzky, and L. Anand, *J. Mech. Phys. Solids*, **70**, 1 (2014).
36. M. J. Welland, D. Karpeyev, D. T. O'Connor, and O. Heinonen, *ACS Nano*, **9**, 9757 (2015).
37. D. Gaston, C. Newman, G. Hansen, and D. Lebrun-Grandie, *Nucl. Eng. Des.*, **239**, 1768 (2009).
38. M. E. Gurtin, *Phys. D*, **92**, 178 (1996).
39. B. Han, A. Van der Ven, D. Morgan, and G. Ceder, *Electrochim. Acta*, **49**, 4691 (2004).
40. Y. C. Song, Z. Z. Li, A. K. Soh, and J. Q. Zhang, *Mech. Mater.*, **91**, 363 (2015).
41. M. Huttin, "Phase-field modeling of the influence of mechanical stresses on charging and discharging processes in lithium ion batteries." *Ph.D. Thesis*, Karlsruhe Institute of Technology, Karlsruhe (2014).
42. T. Zhang and M. Kamlah, *Electrochim. Acta*, **298**, 31 (2019).
43. M. Tang, J. F. Belak, and M. R. Dorr, *J. Phys. Chem. C*, **115**, 4922 (2011).
44. R. Malik, D. Burch, M. Bazant, and G. Ceder, *Nano Lett.*, **10**, 4123 (2010).
45. C. Delacourt and M. Safari, *Electrochim. Acta*, **56**, 5222 (2011).
46. T. Maxisch and G. Ceder, *Phys. Rev. B*, **73**, 174112 (2006).
47. M. Wagemaker, D. P. Singh, W. J. Borghols, U. Lafont, L. Haverkate, V. K. Peterson, and F. M. Mulder, *J. Am. Chem. Soc.*, **133**, 10222 (2011).
48. N. Shpigel, S. Sigalov, M. D. Levi, T. Mathis, L. Daikhin, A. Janes, E. Lust, Y. Gogotsi, and D. Aurbach, *Joule*, **2**, 5 (2018).